UCSF

Title

Chronic kidney disease and aging differentially diminish bone material and microarchitecture in C57Bl/6 mice

Permalink

https://escholarship.org/uc/item/6sp3p3mz

Authors

Heveran, Chelsea M
Schurman, Charles A
Acevedo, Claire
et al.

Publication Date

DOI

Peer reviewed

Chronic kidney disease and aging differentially diminish bone material and microarchitecture in C57Bl/6 mice

Chelsea M. Heveran[1], **Charles Schurman**[2,*], **Claire Acevedo**[3], **Eric W. Livingston**[4], **Danielle Howe**[5], **Eric G. Schaible**[6], **Heather Hunt**[7], **Adam Rauff**[8], **Eve Donnelly**[7,#], **R. Dana Carpenter**[9], **Moshe Levi**[10], **Anthony Lau**[5], **Ted Bateman**[4], **Tamara Alliston**[2,*], **Karen B. King**[11], **Virginia L. Ferguson**[1]

[1]Department of Mechanical Engineering, University of Colorado, Boulder, CO

[2]Department of Orthopaedic Surgery, University of California, San Francisco, CA

[3]Department of Mechanical Engineering, University of Utah, Salt Lake City, UT

[4]Department of Biomedical Engineering, University of North Carolina, Chapel Hill, NC

[5]Department of Biomedical Engineering, The College of New Jersey, Ewing, NJ

[6]Advanced Light Source, Lawrence Berkeley National Laboratory, Berkeley, CA

[7]Department of Materials Science & Engineering, Cornell University, Ithaca, NY

[8]Department of Bioengineering, University of Colorado, Denver, CO

[9]Department of Mechanical Engineering, University of Colorado, Denver, CO

[10]Department of Biochemistry and Molecular and Cellular Biology, Georgetown University, Washington D.C.

[11]Department of Orthopaedics, University of Colorado School of Medicine, Aurora, CO

[*]University of California Berkeley – University of California San Francisco Graduate Program in Bioengineering, San Francisco, CA

[#]Research Division, Hospital for Special Surgery, New York, NY

Abstract

Chronic kidney disease (CKD) is a common disease of aging and increases fracture risk over advanced age alone. Aging and CKD differently impair bone turnover and mineralization. We thus hypothesize that the loss of bone quality would be greatest with the combination of advanced age

Disclosures

No authors have conflicts of interest to disclose.

and CKD. We evaluated bone from young adult (6 mo.), middle-age (18 mo.), and old (24 mo.) male C57Bl/6 mice three months following either 5/6th nephrectomy, to induce CKD, or Sham procedures. CKD exacerbated losses of cortical and trabecular microarchitecture associated with aging. Aging and CKD each resulted in thinner, more porous cortices and fewer and thinner trabeculae. Bone material quality was also reduced with CKD, and these changes to bone material were distinct from those due to age. Aging reduced whole-bone flexural strength and modulus, micrometer-scale nanoindentation modulus, and nanometer-scale tissue and collagen strain (small-angle x-ray scattering (SAXS)). By contrast, CKD reduced work to fracture and variation in bone tissue modulus and composition (Raman spectroscopy), and increased percent collagen strain. The increased collagen strain burden was associated with loss of toughness in CKD. In addition, osteocyte lacunae became smaller, sparser, and more disordered with age for Sham mice, yet these age-related changes were not clearly observed in CKD. However, for CKD, larger lacunae positively correlated with increased serum phosphate levels, suggesting that osteocytes play a role in systemic mineral homeostasis. This work demonstrates that CKD reduces bone quality, including microarchitecture and bone material properties, and that loss of bone quality with age is compounded by CKD. These findings may help reconcile why bone mass does not consistently predict fracture in the CKD population, as well as why older individuals with CKD are at high risk of fragility.

Keywords

CKD; aging; bone quality; bone fragility; collagen

1. Introduction

Chronic kidney disease (CKD) affects an estimated 23–36% of the elderly population and is associated with increased risk of fracture and fracture-related mortality (1,2). Though loss of bone mass (as measured by dual-energy x-ray absorptiometry) predicts future fracture at all stages of CKD, older individuals with low bone mass and CKD are more likely to fracture compared to those with low bone mass and healthy kidney function (3). Bone fracture risk is generally increased with CKD over the effects of aging alone (4,5). For example, in a three-year study, individuals 40–65 with moderate to end-stage CKD had a 1.7 – 5.1 fold increase in fracture prevalence compared with age-matched controls while for those ages 65+, CKD continued to increase the incidence of fracture 1.8 – 4.3 fold over controls (4).

The increased fracture risk with CKD may be explained by a combination of abnormal bone quantity as well as *bone quality* – tissue microarchitecture, geometry, and material properties that together determine bone fracture resistance. CKD commonly alters bone tissue turnover and mineralization, both of which can affect bone quality (6–8). Previous studies in rodents have reported that high-turnover CKD, the topic of the present investigation, affects cortical bone quality, including increased cortical porosity (9), decreased bone mineralization (10,11), decreased microscale tissue modulus (10), altered hydroxyapatite crystal morphology and perfection (11), decreased bound water (12), decreased enzymatic skeletal crosslinks (12) and increased pentosidine (11,12). The impact of CKD on trabecular bone is less consistent; some studies indicate that high-turnover CKD deleteriously affects

trabecular bone microarchitecture (10,13), while others report no changes compared with control (9). Though these studies vary in the species and strain of rodent, method of induction of CKD, and outcomes measured, these prior works provide substantial evidence that CKD alters bone quality.

Several key questions remain about how bone quality is diminished by CKD, the extent to which diminished bone quality is due to defects in the mineral *vs* organic phase, as well as how changes to bone quality influence loss of bone tissue toughness. Notably, though a few studies have identified changes to collagen crosslinks and tissue maturity (*i.e.,* time since bone formation) in CKD, it is unknown if nanoscale interactions of collagen fibers during mechanical loading are altered by CKD and whether these changes in nanomechanics influence whole-bone toughness (11,12). More broadly, an assessment of changes to bone quality and mechanics in response to CKD from nano- to whole-bone length scales has not yet been reported.

The role of the osteocyte in influencing bone quality in CKD and aging is also uncertain. These cells behave abnormally by substantially elevating FGF23 expression early in CKD progression (7,14). The osteocyte is essential for maintaining bone material quality and for regulating bone fracture resistance (15–17). Osteocyte health is indicated, in part, through the lacunar morphology. Osteocyte lacunar morphologies are altered when the osteocyte participates in mineral homeostasis, as in lactation (18,19) and x-linked hypophosphatemia (20). Lacunar geometries can also become smaller, sparser, and more disordered with both aging and disuse (21–23). Changes to osteocyte lacunar morphology with CKD have the potential to affect bone tissue strains, structural integrity, and osteocyte mechanosensitivity (24). It is not yet known if CKD affects osteocyte lacunar morphologies and whether such a relationship may change with aging.

Although the more common CKD populations include older adults, the combined effects of aging and CKD on bone quality have yet to be explored. Prior work has established that aging decreases whole-bone modulus, strength, and work to fracture in bending (25), fracture toughness (26), cortical and trabecular bone microarchitecture (27–29), and increases mineral content and maturity (30,31). These changes to bone with aging are confounding and occur across multiple length-scales, with whole-bone mechanics influenced by changes to bone tissue material as well as structure. Age-related changes to bone material and bone volume are in part influenced by decreased bone tissue turnover (*i.e.,* higher tissue maturity) and a negative balance in the bone multicellular unit, respectively (30,32). Such age-related changes contrast the abnormal bone turnover and mineralization that often occurs with CKD. Loss of microarchitecture is related to negative balance, which is expected with aging and may occur in CKD (9,10,13). However, tissue maturity increases with aging and decreases in the context of high-turnover CKD. Substantial gaps exist in understanding the basis of bone fragility in CKD, as well as how aging and CKD, when combined, reduce bone quality and fracture resistance. Elucidating the combined effects of aging and CKD on bone quality would fill these knowledge gaps.

The purpose of this study was to investigate the combined influences of aging and CKD on bone quality, from nano-through whole-bone length scales, in a surgical model of CKD in

aging mice. We hypothesized that CKD and aging each reduce bone quality, but that these two factors would differentially and negatively influence bone tissue material properties. We further hypothesized that the combined effects of old age and CKD are most detrimental to bone quality. To evaluate these hypotheses, we assessed bone quality, including cortical and trabecular microarchitecture and cortical bone material properties, in young adult though old mice with CKD induced by 5/6th nephrectomy (5/6 Nx) or Sham surgeries.

2. Methods

2.1 Animal model and sample preparation

Male C57Bl/6 mice were obtained from a National Institute on Aging colony at the ages of 3, 15, and 21 months. Mice were maintained on a 12-h light / 12-h dark cycle, housed individually in polycarbonate cages with standard bedding, fed Harlan Teklad 2920X chow, and allowed free access to water. For each of the three ages, mice were randomly assigned to CKD or Sham groups. The CKD group underwent two-stage nephrectomy. These procedures were described previously (33). Briefly, the left kidney was accessed *via* midline incision, decapsulated to avoid ureter and adrenal damage, and then removed. One week later, the right kidney was decapsulated and the upper and lower poles were partially resected to achieve 2/3 reduction in kidney volume. The control group received Sham procedures (*i.e.,* midline incision with no damage to kidneys) within the same timeframe. Mice were anesthetized using 1.5% isoflurane during procedures. A post-operative dose of buprenorphine (0.5 mg/kg) was administered after these procedures and prior to recovery, as well as every 12 hours for the next two days. Mice were euthanized after three months *via* CO_2 and cervical dislocation. At the study endpoint, mice were 6 (young adult; Sham: n = 6, CKD: n = 7), 18 (middle-age; Sham: n = 8; CKD: n = 10), and 24 (old; Sham: n = 8; CKD: n = 8) months of age. All animal procedures were approved by the Institutional Animal Use and Care Committee at the University of Colorado Denver.

The left femur, tibia, humerus, radius, and ulna were reserved for bone quality analyses. The left tibia was preserved in 70% ethanol at 4° C. All other bones were wrapped with phosphate-dampended gauze and stored at −20° C until analysis.

2.2 Serum and urine chemistries

Serum biochemistry analyses were performed on blood and urine collected at the study endpoint. Serum and urine urea as well as serum phosphate, calcium, and PTH concentrations were measured according to manufacturer's directions (BioAssays Systems and Immunotropics, respectively).

2.3 microCT

Microarchitecture was assessed for the cortical bone of the midshaft femur and trabecular bone of the proximal tibia using microCT for all study mice (μCT, Scanco 80, Scanco AG, Basserdorf, Switzerland). Femurs were defrosted overnight at 4° C before scanning. Scanning was performed with 10 μm voxel size, following acquisition and analysis methods described previously (10). Cortical parameters included bone volume / total volume (BV/TV), bone area / total area (BA/TA), cortical porosity (Ct.Po), cortical thickness (Ct.Th),

total mineral density (TMD), moment of inertia about the medial-lateral axis (I_{ML}), distance between the centroid and bone surface in the anterior-posterior direction (C), and polar moment of inertia (pMOI) (34). Trabecular parameters included trabecular number (Tb.N), trabecular spacing (Tb.Sp), trabecular thickness (Tb.Th), bone volume (BV), total volume (TV), bone volume / total volume (BV/TV), volumetric bone mineral density (vBMD), and connectivity density (Conn.D). Following microCT, femurs were again wrapped in phosphate-dampened gauzed and stored at −20° C for subsequent whole-bone mechanical characterization.

2.4 Whole-bone mechanical and material properties

Following microCT, left femurs underwent three-point bending (Insight II Material Testing System, 250 N load cell, MTS Systems Corporation, Eden Prairie MN). Femurs were removed from phosphate-buffered saline-dampened gauze and tested to failure using a deflection rate of 5 mm/min on a custom anvil with 8 mm span. Load-displacement curves were analyzed for mechanical properties including stiffness, maximum load, displacement at maximum load, energy at maximum load, load at yield, displacement at yield, energy at yield, post-yield displacement, load at fracture, displacement at fracture, and energy at fracture. The yield point was defined as the intersection of a secant line drawn with a 10% reduction in slope from the initial tangent stiffness and the load-displacement curve. Using I_{ML} and C from μCT, we estimated material properties including bending modulus, yield stress, ultimate stress, and toughness from the three-point bending data using standard beam bending equations as applied to the mouse femur (35).

2.5 Finite element analysis of stiffness of the proximal tibia

To investigate the mechanical behavior of bone, computational finite element (FE) modeling was used to simulate axial compression of the proximal tibia in each model. The proximal tibia was chosen because the tibia is a load bearing structure in mice and is a common site of analysis of bone properties using microCT. MicroCT image data of the proximal tibia (cortical and trabecular bone) was exported as 16-bit DICOM image slices for further segmentation and construction of the subject specific Finite Element Models. DICOM image data was imported into Mimics Innovation Suite 18 (Materialise, Leuven Belgium) for image processing and segmentation to create a corresponding FE model for the same proximal tibia region of the bone analyzed with microCT. Bone tissue was separated from other tissues in the image by using a segmentation threshold of 313 mgHA/cm^3 (36,37). Once the bone region was segmented, the subject specific FE mesh was exported, which contained both the cortical and trabecular compartments. The FE model used a hexahedral FE mesh with a 10 μm isotropic element size.

The FE meshes exported from Mimics were imported into ABAQUS CAE 6.9 for assignment of material properties, application of boundary conditions, and simulation of axial mechanical loading. The material properties of the bone were specified to be homogenous, isotropic, and linear elastic (Young's Modulus, $E = 10$ GPa and Poisson's Ratio, $v = 0.3$). To simulate axial compression, a fixed boundary condition was applied to the nodes at the inferior surface of the bone, and a downword displacement of 5μm (0.5% of height of bone segment) was applied to the nodes on the superior surface of the bone. Bone

structural stiffness was calculated as the reaction force (N) over the applied displacement (mm).

2.6 Small-angle x-ray scattering

Collagen fibril deformation during uniaxial tension testing of combined ulnae and radii was measured using synchrotron small-angle x-ray scattering (SAXS) at beamline 7.3.3 at the Advanced Light Source (LBNL, Berkeley, CA) (38). Bones were secured with glue and sandpaper between clamps at their distal and proximal ends. *In situ* tensile tests were performed with a TST350 Tensile Testing Stage (Linkam Scientific Inc.) on hydrated samples at a displacement rate of 2.5 μm/s. During testing, the bone diaphysis was exposed to X-rays of 10 keV for 0.1 s every 5 s. Total radiation was limited to 30 kGy to mitigate any exposure effects on mechanical performance (39). The collagen *d*-spacing, representative of the repeating gap regions within the collagen super-structure, appears as a prominent Bragg diffraction peak in the SAXS pattern. Collagen specific deformation throughout tensile testing was measured by tracking the shift in the Bragg peak positions at increasing amounts of load. Utilizing a custom LabVIEW program, this progressive change in the scattering pattern was converted to collagen fibril strain by normalizing to the *d*-spacing at zero load, as discussed previously (40). Tissue stress was calculated from forces recorded on the testing stage divided by the cross-sectional area measurements of the bones tested. The summed cross-sectional areas of the ulna and radius were measured from the mid-point of the ulnar length using brightfield reflective imaging (Leica DM, 20x objective) and quantified with ImageJ (41). Whole-bone tissue strains were obtained with a custom Digital Image Correlation (DIC) MATLAB package which tracked and measured distances between a grid of points overlaid on the bone specimen throughout testing. The DIC obtained strains were combined with tissue-level stresses to generate standard stress-strain curves. Linear elastic modulus was extracted from these curves as well as yield stress and yield strain as defined by the 0.2% offset yield point. Tissue strain was time-matched to collagen strains from SAXS at yield and max stress in order to produce comparisons of stress-carrying components with bone during deformation.

Controlled analysis of the ulna/radius composite during the tensile test was performed by matching the tissue-level strain from the digital camera images to the strains calculated to from the X-ray scattering patterns. Digital videos were independently reviewed by two trained observers for fracture and tissue slip (*e.g.*, slip between the ulna and radius). These events were then time-matched to the strain curves and all stress-strain data were truncated to the first fracture. Only data until the first fracture were considered in the analysis. Specimens were excluded if there was slip between the tensile grips and the bones, or if there was slip between the radius occurring before the first fracture. Specimens were also excluded if there was poor correspondence between tissue and SAXS strain curves, which indicates that the beam spot was focused on the ulna but the majority of the strain was transferred to the radius.

2.7 Site-matched assessment of microscale bone tissue composition and modulus

Following three-point bending, femurs were histologically dehydrated in a graded series of ethanol, cleared in acetone, and embedded in PMMA. Embedded bones were sectioned at

the femoral midshaft using a low speed diamond saw (Isomet, Buehler, Lake Bluff, IL). Specimens were ground using wet silicon carbide paper (600 and 1200 grit), and then polished with alumina pastes (9, 5, 3, 1, 0.1, 0.05 μm) and Rayon fine clothes (South Bay Technologies, San Clemente, CA) to a final finish of 0.05 μm. Samples were sonicated between each polishing step.

Raman spectroscopy was performed in maps spanning the cortical thickness with a custom system: a Renishaw inVia confocal microscopy system (Renishaw, Wotton-under-Edge, Gloucestershire, UK) using 785 nm wavelength laser light that was routed through fiberoptic cables to a 50x objective (NA 0.75) mounted on a nanoindenter z-stage (TI 950, Hysitron, Minneapolis, MN). For each location, 10 accumulations of 10 second exposures were collected. Rows of three indents spaced 15 μm apart extended every 10 μm through the cortical thickness.

The fluorescent baseline was subtracted with an 11th order polynomial fit, and cosmic rays were removed using the Renishaw WIRE software. A reference PMMA spectrum was subtracted from each point using custom MATLAB code. These corrected spectra were then analyzed for proline (855 cm^{-1}), ν_1 phosphate (961 cm^{-1}), and ν_1 carbonate (1071 cm^{-1}). Area ratios were then calculated for mineral:matrix (phosphate:proline), carbonate:phosphate, and crystallinity (inverse of half-width at full maximum height of the ν_1 phosphate peak).

Nanoindentation was then performed at locations matched to sites evaluated with Raman spectroscopy. A 5 μm spherical tip indented the bone at 30 nm/s until a maximum depth of 500 nm was obtained. This depth was maintained for 120 s to allow dissipation of viscoelastic energy. Reduced modulus (E_r) was calculated using Oliver-Pharr analysis, considering the first 45% of the unloading curve (42,43).

2.8 High-performance liquid chromatography

The humerus was dissected of all soft tissue, and bone marrow was removed with water. Humeri were C, and then centrifuged to evaporate excess HCl. Filtered samples were diluted 1:5 in 10 % acetonitrile and 0.05 % heptafluorobutyric acid (HFBA), loaded onto a reverse-phase Gemini-NX C-18 column (Phenomenex, Torrance, CA) and analyzed for crosslinks hydroxylysylpyridinoline (HP), lysyl pyridinoline (LP), and pentosidine consistent with methods described by Bank *et al* (44). Details of the HPLC system (model 126, Beckman-Coulter, Fullerton, CA) are described at length in Oren *et al* (45). Separation of collagen crosslinks involved the following protocol: 15 min. of solvent containing 24% methanol and 0.15% HFBA, 10 min. of solvent containing 40% methanol and 0.05% HFBA, and 10 min. of solvent containing 75% acetonitrile and 0.1% HFBA. The column was equilibrated in 24% methanol and 0.15% HFBA for at least 10 min. between sample runs. Collagen crosslink peaks were measured with a fluorescence detector (FP1520, JASCO; Easton, ML). Excitation and emission wavelengths were 295 nm and 400 nm, respectively, for HP and LP. Pentosidine was detected with 328 nm excitation and 378 nm emission. Calibration curves were generated from the measured intensities of five dilutions of a calibrator containing purified HP and LP (Quidel Corportation) and pentosidine (L. Sayre, Case Western Reserve University, Cleveland, OH).

Crosslink concentrations were then normalized to concentration of collagen. Collagen was estimated from the concentration of hydroxyproline within the sample analyzed for crosslinks. An aliquot of the sample analyzed for crosslinks was diluted 1:50 and derivatized with 9-fluoronylmethyl chloroformate (46). The following solutions were used for the amino acid protocol (1) 20 mM citric acid, 5 mM tetramethylammonium chloride, and 0.01% sodium azide, pH 2.85; (2) 20 mM sodium acetate, 5 mM tetramethylammonium chloride, and 0.01% sodium azide, pH 4.5, and (3) 100% acetonitrile. The gradient elution profile follows: from 0–11.5 min. a gradient of 75% (1) / 25 % (3) to 60% (1)/40% (3), at 13 min. switch to 64% (2) / 36% (1), from 13.1 –18 min. a gradient of 64% (2) / 36% (3) to 62% (2) / 38%(3), then at 18 min. a switch to 25% (2) / 75% (3) until the end of the run at 23 min.. The column was equilibrated in 75% (1) / 25% (3) for at least 10 min. between sample runs. Amino acid peaks were monitored at 254 nm excitation and 630 nm emission. A calibration curve was generated from five dilutions of an amino acid standard prepared from collagen hydrolysate (Sigma-Aldrich #A9531, St. Louis, Missouri). Collagen has a constant concentration of hydroxyproline, thus hydroxyproline concentration was converted to concentration of collagen (285 mol hydroxyproline per mol collagen).

2.9   Measurement of Fluorescent AGEs

Fluorescent AGEs in each specimen were determined by a fluorometric assay that compares the bulk endogenous fluorescence of the bone tissue to a quinine standard. An aliquot of the hydrolyzed bone resuspended with internal standard for HPLC was diluted with DI water to a concentration of 1.6 μg bone/ml solution. The fluorescence of the diluted hydrolysate and a serially diluted stock solution of quinine (stock: 10 μg quinine/ml 0.1 N H_2SO_4) were measured in a 96-well plate (Product #3370, Corning) using a multi-mode microplate reader (Synergy H1, BioTek) at an excitation of 360 nm and an emission of 460 nm.

Bulk fluorescent AGEs were normalized to the collagen content of the bone tissue using a colorimetric assay of hydroxyproline. Briefly, the hydrolysate was further diluted to a c c μ / ed stock solution of hydroxyproline (200 μg L-hydroxyproline/ml 0.001 N HCl). Chloramine-T was added to the diluted hydrolysate to initiate the reaction, and the solutions were incubated for 20 min. at room temperature. The reaction was stopped by addition of 3.15 M perchloric acid, and after a 5-min. incubation period at room temperature, p-dimethylaminobenzaldehyde was added. Next, the solution was incubated in a 60 °C water bath for 20 min., then cooled in cold water in darkness to room temperature. The absorbance of the specimens and standards was measured at a wavelength of 570 nm using a microplate reader. Fluorescent AGEs are reported in units of ng quinine fluorescence/mg collagen.

2.10   3D osteocyte lacunar geometries

The left tibia was histologically dehydrated in a graded series of ethanol and stained with 1% basic fuchsin (47). Tibiae were then cleared with acetone and embedded in poly(methyl)methacrylate (PMMA). Embedded samples were transversely sectioned 1 mm proximal to the tibia-fibula junction with a low-speed saw (Buehler Isomet, Buehler, Lake Bluff, IL). A ground section was prepared from the distal section with target thickness of 200 um (Exakt 400 CS, Exakt Technologies Inc, Oklahoma City, OK).

Imaging of ground sections was performed in transmission with a Zeiss LSM 710 confocal laser scanning microscope, with 555 nm excitation, 568–1000 nm bandpass filter, and 40x oil-immersion objective. Resolution in x, y, and z directions was 0.447 and 0.493 μm, respectively. Vertical z-stacks were obtained through the visible range of osteocyte lacunae (50–100 μm of imaging depth).

3D images of osteocyte lacunae were constructed and analyzed for lacunar geometries using the open-source 3D Osteocyte Lacunae Analysis program and MATLAB v17 (21). Briefly, each 2D image within a z-stack was automatically segmented to define lacunae, which were then reconstructed in 3D. Based on best-fit ellipsoids, lacunae were analyzed for volume, surface area, closest center of mass, sphericity (ratio of smallest to largest lacunar radii, where 1 = sphere), span theta (absolute value of the difference of the 3D vector describing the major axis direction from the average direction of all lacunae), oblateness (−1 = perfectly prolate, 1 = perfectly oblate), and lacunar number density (number of osteocytes / image volume).

2.11 Data analysis

Data are presented as mean ± standard error of the mean. For each array from Raman spectroscopy and nanoindentation were averaged such that each bone had one value for each microscale measure. Similarly, a standard deviation was calculated for each array to estimate microscale bone tissue spatial variability. The effects of aging and CKD, as well as their interaction, were tested with two-way ANOVA for all parameters. Dependent variables were transformed if necessary to satisfy assumptions of residual normality and homoscedasticity. Significance for main effects was set *a priori* to $p < 0.05$. In the case of a significant interaction between age and CKD, post-hoc testing was performed to test the effect of CKD within each age. Family-wise error was controlled for these post-hoc analyses using Bonferroni-adjusted alpha, which resulted in a critical alpha of $0.05 / 3 = 0.017$. Results where simple effects comparisons had p-values between 0.017 and 0.05 were interpreted as non-significant.

Linear regression was performed to test whether nano-microscale bone quality measurements predict whole-bone mechanical toughness. Because whole-bone mechanical properties show strong dependence on age, this linear regression included age as a covariate. Spearman correlations were also assessed for osteocyte lacunar geometries and measures from serum and urine chemistry, and for PTH and measures of microscale bone quality. Significance for linear regressions and correlations was set at $p < 0.05$. Minitab (v17) was used for all analyses.

Outliers were identified *via* Grubbs test (significance level = 0.05). Several outliers were excluded from serum calcium and urea analyses. An outlier each for 24-month Sham and CKD was excluded for all cortical and trabecular microarchitecture analyses, as well as FEA analysis. One outlier was excluded from the 24-month CKD group for LP analysis, and one outlier was excluded for the 24-month Sham group for toughness, work to fracture, and post-yield displacement. One separate 24-month Sham outlier was found for standard deviation of nanoindentation modulus and standard deviation of crystallinity.

3. Results

3.1 Confirmation of kidney disease

At the study endpoint three months from surgery, mice with 5/6 Nx had significantly elevated serum urea and diminished urine urea, consistent with impaired kidney function (Table 1). Serum PTH and phosphate were significantly increased as main effects of CKD. Serum calcium was not significantly affected by CKD. For all serum and urine measures, age was not a significant main effect.

3.2 Aging and CKD reduce cortical and trabecular microarchitecture

Aging and CKD both negatively affected cortical geometry and trabecular microarchitecture (Tables 2 – 3, Figure 1). Aging from 6 mo. to 24 mo. significantly increased cortical bone cross-sectional dimensions (increased polar moment of inertia, pMOI), porosity (Ct.Po) and tissue mineral density (TMD), and decreased cortical bone thickness (Ct.Th), cortical bone volume (decreased bone volume fraction (BV/TV), bone area fraction (BA/TA). Aging also reduced trabecular number (Tb.N) and thickness (Tb.Th), trabecular bone volume fraction (BV/TV), and volumetric bone mineral density (vBMD). As with aging, CKD also had a significant negative main effect on bone volume *via* decreased BV/TV, Tb.N, BA/TA, Ct.Th, and increased Ct.Po. These effects were additive, such that the worst bone volume was observed for old mice with CKD. Unlike aging, CKD significantly decreased pMOI and TMD. Aging and CKD did not have a significant interaction for any cortical or trabecular microarchitecture measure.

3.3 Aging and CKD differently diminish whole-bone mechanical and material properties

At the whole-bone level, material and mechanical properties were both diminished by aging and CKD (Table 4, Supplementary Table 1). Aging from 6 mo. to 24 mo. significantly reduced most whole-bone material properties (*e.g.,* modulus, yield stress, maximum stress) but did not affect toughness. CKD significantly reduced work to fracture, but most other material and mechanical parameters were not affected by CKD as a main effect. Toughness, the geometry-independent analog of work to fracture, had a significant interaction between aging and CKD ($p = 0.011$). From post-hoc testing, it was seen at 18 mo that CKD may lower toughness (-47.9%, $p = 0.023$) (Figure 2d).

3.4 Aging and CKD reduce FEA structural stiffness at the proximal tibia

We utilized FEA in order to evaluate how aging and CKD affect mechanical properties *via* changes to trabecular and cortical structure. FEA structural stiffness at the proximal tibia significantly decreased with aging and CKD (Table 4). There was not a significant interaction between aging and CKD. FEA stiffness positively correlated with femoral stiffness from three-point bending ($r^2 = 0.67$).

3.5 Aging lowers microscale bone stiffness while CKD reduces microscale bone tissue spatial variation

In order to assess how aging and CKD affect tissue-scale material properties of cortical bone, we employed nanoindentation and Raman spectroscopy at matched sites to evaluate

microscale bone tissue modulus and composition (Table 5). Bone tissue heterogeneity was evaluated through assessment of spatial variance of these properties. Mean reduced modulus (E_r) and the standard deviation of E_r were significantly decreased and increased, respectively, with age. CKD significantly reduced the standard deviation, but not the mean, of E_r. Microscale bone tissue composition assessed by Raman spectroscopy (*i.e.,* mean mineral:matrix, carbonate:phosphate, crystallinity) did not significantly change with either age or CKD. However, the standard deviation of crystallinity was significantly reduced with CKD.

3.6   Aging and CKD differently affect collagen fibril nanomechanics

We evaluated whether CKD and aging affect collagen nanomechanics *via* small-angle x-ray scattering (SAXS) concurrent with tensile loading. In agreement with results from bending, tensile measurements demonstrated that aging significantly reduced tissue yield stress and max stress. Collagen nanomechanics were affected differently by age and CKD (Table 6, Figure 2). Aging reduced the collagen strain measured at maximum tissue strain but did not affect the percent collagen strain (collagen strain / total tissue strain, %ColMax). By contrast, CKD significantly increased the %ColMax.

3.7   Collagen crosslinks did not differ with aging and CKD

We sought to understand whether the altered collagen nanomechanics observed in CKD could be attributed to changes in skeletal crosslinks. We therefore characterized enzymatic (hydroxyl lysyl pyridinoline, HP, and lysyl pyridinoline, LP) and non-enzymatic crosslinking (pentosidine) with high-performance liquid chromatography (HPLC). The crosslinks HP, LP, and pentosidine had higher mean concentrations with increasing age, but these changes were not significant (Table 7). Similarly, there was a trend of lower LP with CKD, but this effect was not significant. We further quantified total fluorescent advanced glycation end-products (AGEs) and found that total fluorescent AGEs did not differ with aging or CKD.

3.8   Age-related osteocyte lacunar geometry changes are not observed in aging mice with CKD

Osteocyte perilacunar/canalicular remodeling (PLR) responds to changes in mineral homeostasis and is important in determining bone fracture resistance. We evaluated osteocyte lacunar geometry to determine whether aging with CKD alters PLR (Table 8). The effects of aging alone (without CKD) for these Sham mice were reported previously (21). Briefly, for Sham mice, lacunae became smaller, more spherical, and less numerous with increased age. When aging and CKD were analyzed together for the present study, aging significantly decreased lacunar number density, volume, and surface area, and increased sphericity, oblateness, and span theta. There was not a significant effect of CKD for any measure. However, there was a significant interaction between age and CKD for sphericity. While sphericity increased with age for Sham mice, this measure was greatest for middle-age mice with CKD and then decreased for old mice to a value similar to that observed in young mice. In other words, lacunae became smaller and rounder only in aging Sham mice, and not in aging mice with CKD. This pattern was also observed with CKD for lacunar

number density, volume, and surface area, although the interaction between aging and CKD was not significant.

Osteocyte lacuna size did not increase with age for mice with CKD, but instead increased with phosphate dysregulation. Specifically, for mice with CKD, osteocyte lacunar volume (Spearman $\rho = + 0.584$, $p = 0.017$), surface area ($\rho = + 0.603$ $p = 0.013$), and sphericity ($\rho = - 0.500$, $p = 0.048$) were correlated with serum phosphate assessed at the study endpoint. By contrast, measures related to lacunae prevalence and orientation (*i.e.,* osteocyte number density, closest center of mass, span theta) did not significantly correlate with circulating phosphate. No osteocyte lacunar measurements were significantly correlated with serum calcium, serum urea, or urine urea. For Sham mice, osteocyte lacunar number density was positively correlated with serum calcium ($\rho = +0.681$, $p = 0.004$). All other osteocyte lacunar measurements only weakly correlated with serum and urine chemistry.

The relationship between osteocyte lacuna size and serum phosphate for mice with CKD was not directly caused by increased PTH. When considering Sham and CKD mice together, phosphate significantly correlated with increased PTH (Spearman $\rho = +0.562$, $p = 0.001$). However, although phosphate and PTH were both increased as a main effect of CKD, these measures were not significantly correlated with each other for CKD mice ($p > 0.05$). No measures of osteocyte lacunar geometry significantly correlated with PTH for Sham or CKD mice.

3.9 Regression analysis reveal that altered collagen nanomechanics influence toughness

We sought to identify how changes to whole-bone toughness from bending were related to changes in nano-to microscale measures of bone quality for Sham and CKD mice. We performed regression of whole-bone toughness *vs* bone quality measures at smaller length-scales for Sham and CKD mice using age as a covariate. For Sham mice, no bone quality measures were significant explanatory variables for toughness. For CKD, the only significant predictor of toughness (T) was %ColMax ($\ln(T) = 2.437 - 0.00371*\%ColMax$; $r^2 = 49.4\%$, $p < 0.05$). The strength of the regression was not improved by adjusting for age.

3.10 Bone quality changes are not explained by variation in PTH

We assessed Spearman correlations between bone quality measures and PTH to understand if mice with higher PTH had worse bone quality. Though PTH was significantly higher with 5/6 Nx, there were no significant correlations between PTH and microscale bone quality.

4. Discussion

The purpose of this study was to investigate how 5/6 Nx – induced CKD and aging each diminish bone quality, including bone microarchitecture as well as bone tissue material properties. CKD reduced bone quality, including microarchitecture and material, from the micrometer-length scale to the whole-bone scale. In our study, bone quality declines were observed across several modalities and length-scales. The effect of CKD was to diminish cortical and trabecular microarchitecture, alter spatial variation in microscale material properties, and also to alter collagen nanomechanics. Additionally, CKD and aging had an interactive effect on toughness that was greatest for middle-age mice. Our results highlight

that several key components of bone quality are impaired in CKD. These observations support a growing body of evidence from rodent and clinical studies that bone quality is reduced in CKD and likely contributes to loss of fracture resistance.

The loss of bone microarchitecture with CKD occurred in addition to the deleterious effects of aging and contributed to loss of whole-bone strength. In this study, we found that aging and CKD both significantly diminished cortical and trabecular microarchitecture. Aging and CKD each resulted in thinner, more porous cortical bone, and fewer and thinner trabeculae. The only exception was bone mineral assessed by microCT (*i.e.,* TMD), which increased with age and was diminished in CKD. For all cortical and trabecular metrics, the worst bone microarchitecture was apparent in old mice with CKD. The loss of bone microarchitecture influenced whole-bone structural integrity. From FEA, it was found that aging reduced bone microarchitecture at the proximal tibia while CKD reduced structural stiffness.

For measures relating to bone material quality, age and CKD had differing effects (Figure 2). With increased age, whole-bone modulus and maximum stress were both reduced, as was micrometer-scale tissue modulus. Yield and maximum stress from tensile testing of the ulna-radius also decreased with age. Further, consistent with human samples studied with SAXS, aging was associated with increased collagen strain at maximum strain, implying a stiffening of collagen fibers (26). CKD did not affect whole-bone modulus or strength, but instead significantly reduced work to fracture, and altered tissue-scale material spatial variation. Further, CKD may reduce toughness in middle-age mice, as with this disease the burden of tensile strain was shifted to collagen fibers. Increased percent collagen at maximum load was the only significant explanatory variable for reduced toughness in CKD, suggesting that the loss of whole-bone toughness may be at least partially explained by altered collagen mechanics.

The origin of altered collagen nanoscale mechanical behavior is uncertain. There was a trend of lower skeletal crosslinks with CKD. However, HP and LP measured from the humerus did not correlate with collagen mechanical properties from SAXS measured at the ulna/radius complex, perhaps due to different sites of analysis. This shift in strain may also result from altered mineral content or distribution, or from changes to binding between collagen and mineral. Increased %ColMax may not be directly responsible for the loss of toughness in CKD but could be a symptom related to altered turnover and deficiencies in mineral organization. For instance, altered mineralization could render the collagen more mobile, or may dissipate less energy through microcracking. These changes could produce the observed loss of toughness with CKD as well as the increased strain burden on collagen fibers. In future studies it will be important to identify why CKD shifts strain to collagen fibers, but here we note that this change in collagen behavior appears to play an important role in how CKD diminishes whole-bone material properties.

As changes to bone material properties occur with CKD and the osteocyte is known to modulate tissue-scale bone quality through perilacunar/canalicular remodeling (PLR), we also aimed to understand whether 3D osteocyte lacunar morphologies were modified in CKD (15,16). While osteocyte lacunae became smaller, sparser, and less aligned with increased age for Sham mice, lacunae remained prevalent and large for old mice with CKD.

Instead, for mice with CKD, serum phosphate was significantly and positively correlated with osteocyte lacuna size. Although both phosphate and PTH were significantly elevated with CKD, mice with higher PTH did not have higher phosphate. These results are not necessarily discordant. Serum phosphate is the net result of phosphate added from intestinal absorption and bone resorption less phosphate removed by renal excretion and bone formation. Thus, although our CKD mice had generally elevated PTH, those with higher phosphate may have exhausted other systemic compensatory mechanisms.

Osteocytes express greater FGF23 in the context of impaired mineralization (*e.g.*, DMP1 knockout, x-linked hypophosphatemia) (20,48,49) as well as in chronic kidney disease (14,48,50). Recent evidence suggests that in addition to this endocrine role, the osteocyte can directly participate in phosphate mineral homeostasis *via* PLR (20). Osteocyte lacunae volumes were found to increase with x-linked hypophosphatemia. Treatment with either FGF23 or 1,25 dihydroxyvitamin D blocking antibodies restored osteocyte lacunar volumes to values closer to wild type comparisons (20). In CKD, mineral dysregulation is initially spurred by the decreased phosphate filtration of the diseased kidney. Increased bone turnover is a maladaptive response that indicates that systemic compensatory mechanisms for maintaining phosphate control are overwhelmed (6,7). In this case, the relationship between heightened phosphate and increased osteocyte lacunar volume suggests that PLR could be an additional mineral homeostasis regulation strategy. Additional study is required to investigate how osteocyte lacunar geometries and PLR are related to altered bone turnover, bone tissue material quality, and fracture resistance in CKD.

Our findings suggest that processes affecting bone material are different in aging versus CKD. In aging humans as well as mice, bone turnover (*i.e.,* osteoclastic resorption and osteoblastic formation) slows and tissue maturity increases. In this study, 5/6 Nx produced distinct bone quality defects from aging, such as lower bone density from microCT, altered variability of tissue-scale material properties, and greater participation of collagen in tensile loading. Though PTH was significantly higher with CKD, mice with higher PTH did not have lower bone quality. Several reasons may explain this finding. First, mice in our study had much lower PTH than in studies with severe CKD and concomitant secondary hyperparathyroidism (9,12). It is possible that changes in bone turnover were relatively modest in our study. However, we did not directly assess bone turnover, so this possibility is speculative. Second, CKD, regardless of turnover status, has been experimentally associated with altered bone quality. Iwasaki and coworkers reported that high-turnover CKD from 5/6 Nx as well as low-turnover CKD from 5/6 Nx and thyroparathyroidectomy both resulted in similarly altered bone mechanics, and attributed these changes to uremia (11). It is possible that bone quality loss is not predicated solely on secondary hyperphosphatemia but is also influenced by more modest changes in bone turnover and accumulation of uremic toxins.

We expected that several bone quality metrics, including whole bone toughness, pentosidine, mineral:matrix, and carbonate:phosphate would change from 6 to 24 months (25,26,30,51,52). While each of these metrics changed in the expected direction with increased age, the effect of age was not statistically significant. Post-hoc power analysis using G*Power (53) suggests that toughness, pentosidine, and mineral:matrix were underpowered to detect the effect of aging, while carbonate:phosphate was likely not

affected by age in this study. In addition, the collagen crosslink LP was underpowered for detection of an effect of CKD (Supplemental Table 2). There are several possibilities why some measures of bone quality were ultimately underpowered in this study. First, we utilized a custom Raman-nanoindentation instrument with the unique advantage of co-localized measurements. Signal intensity is lower on this custom instrument than standalone Raman instruments, and thus it is possible that our signal:noise ratio was not sufficient to discern age-related changes. Toughness (calculated from work to fracture) is a measure prone to high variability (54), and variability in mechanical properties is increased further for geriatric mice (25). Greater variability in pentosidine has also been observed with increased age in human and rodent studies (52,55,56). Thus it is likely that high variance in these measures obscured differences between evaluated groups.

There were several limitations that influenced outcomes to this study. Dynamic quantitative histomorphometry was not performed, but in future studies would enable evaluation of osteoblast, osteoclast, and osteocyte activities as well as bone turnover. While we identified several bone quality impairments that emerge with CKD and deleteriously affect whole-bone toughness, further work is needed to confirm the origins of these impairments, as well as the role of the osteocyte in their occurrence. Analysis of gene and protein expression would be useful in identifying the origin of impaired collagen nanomechanics, as this impairment was not clearly influenced by changes in collagen crosslinks. Additionally, our interpretation of how the osteocyte may participate in regulating mineral homeostasis and maintaining bone quality in CKD requires additional global (*i.e.,* gene expression) and local measurements (*i.e.,* histological assessment of bone resorption and formation).

In summary, we found that CKD lowers bone quality in addition to the effects of aging alone. CKD and aging similarly reduce cortical and trabecular bone microarchitecture such that the most profound loss of microarchitecture was observed in old mice with kidney disease. CKD also diminished bone material properties, resulting in bone with lowered apparent tissue maturity with altered collagen nanomechanics. These reductions in bone quality, including microarchitecture and bone material properties, provide insight into how fracture resistance is lost in CKD. Further, the combined effects of aging and CKD on bone quality help explain why older individuals with CKD have the highest risk of fracture.

Supplementary Material

Refer to Web version on PubMed Central for supplementary material.

Acknowledgements:

References

1. Nickolas TL, McMahon DJ, Shane E. Relationship between moderate to severe kidney disease and hip fracture in the United States. J Am Soc Nephrol 2006 11;17(11):3223–32. [PubMed: 17005938]

2. Nitsch D, Mylne A, Roderick PJ, Smeeth L, Hubbard R, Fletcher A. Chronic kidney disease and hip fracture-related mortality in older people in the UK. Nephrol Dial Transplant 2009 5;24(5):1539–44. [PubMed: 19075194]

3. Yenchek RH, Ix JH, Shlipak MG, Bauer DC, Rianon NJ, Kritchevsky SB, et al. Bone Mineral Density and Fracture Risk in Older Individuals with CKD. Clin J Am Soc Nephrol 2012;7(March 1997).

4. Naylor KL, Mcarthur E, Leslie WD, Fraser L, Jamal SA, Cadarette SM, et al. The three-year incidence of fracture in chronic kidney disease. Kidney Int 2014;86(4):810–8. [PubMed: 24429401]

5. Kim SM, Long J, Montez-rath M, Leonard M, Chertow GM. J BMR Hip Fracture in Patients With Non-Dialysis-Requiring Chronic Kidney Disease

6. Moe S, Drüeke T, Cunningham J, Goodman W, Martin K, Olgaard K, et al. Definition, evaluation, and classification of renal osteodystrophy: a position statement from Kidney Disease: Improving Global Outcomes (KDIGO). Kidney Int 2006 6;69(11):1945–53. [PubMed: 16641930]

7. Hruska K, Teitelbaum S. Renal Osteodystrophy. N Engl J Med 1999;30(3):773–773.

8. Supplements KI. KDIGO 2017 CLINICAL PRACTICE GUIDELINE UPDATE FOR THE DIAGNOSIS, EVALUATION, PREVENTION, AND TREATMENT OF CHRONIC KIDNEY DISEASE – MINERAL AND 2017;1–59.

9. Moe SM, Chen NX, Newman CL, Gattone VH, Organ JM, Chen X, et al. A comparison of calcium to zoledronic acid for improvement of cortical bone in an animal model of CKD. J Bone Miner Res 2014;29(4):902–10. [PubMed: 24038306]

10. Heveran CM, Ortega AM, Cureton A, Clark R, Livingston EW, Bateman TA, et al. Moderate chronic kidney disease impairs bone quality in C57Bl/6J mice. Bone 2016;86:1–9. [PubMed: 26860048]

11. Iwasaki Y, Kazama JJ, Yamato H, Matsugaki A, Nakano T, Fukagawa M. Altered material properties are responsible for bone fragility in rats with chronic kidney injury. Bone 2015;81:247–54. [PubMed: 26187196]

12. Allen MR, Newman CL, Chen N, Granke M, Nyman JS, Moe SM. Changes in skeletal collagen cross-links and matrix hydration in high- and low-turnover chronic kidney disease. Osteoporos Int 2015 3;26(3):977–85. [PubMed: 25466530]

13. Kadokawa S, Matsumoto T, Naito H, Tanaka M. Original Assessment of Trabecular Bone Architecture and Intrinsic Properties of Cortical bone Tissue in a Mouse Model of Chronic Kidney Disease. J Hard Tissue Biol 2011;20(2):79–86.

14. Stubbs JR, He N, Idiculla A, Gillihan R, Liu S, David V, et al. Longitudinal evaluation of FGF23 changes and mineral metabolism abnormalities in a mouse model of chronic kidney disease. J Bone Miner Res 2012;27(1):38–46. [PubMed: 22031097]

15. Tang SY, Herber RP, Ho SP, Alliston T. Matrix metalloproteinase-13 is required for osteocytic perilacunar remodeling and maintains bone fracture resistance. J Bone Miner Res 2012;27(9):1936–50. [PubMed: 22549931]

16. Dole NS, Mazur CM, Acevedo C, Lopez JP, Monteiro DA, Fowler TW, et al. Osteocyte-Intrinsic TGF-β R Q P c / c R R 2017;21(9):2585–96.

17. Alliston T Biological regulation of bone quality. Curr Osteoporos Rep 2014;12(3):366–75. [PubMed: 24894149]

18. Kaya S, Basta-Pljakic J, Seref-Ferlengez Z, Majeska RJ, Cardoso L, Bromage T, et al. Lactation Induced Changes in the Volume of Osteocyte Lacunar-Canalicular Space Alter Mechanical Properties in Cortical Bone Tissue. J Bone Miner Res 2017;32(4):688–97. [PubMed: 27859586]

19. Bonewald LF. The amazing osteocyte. J Bone Miner Res 2011;26(2):229–38. [PubMed: 21254230]

20. Tokarz D, Martins JS, Petit ET, Lin CP, Liu ES, Program M, et al. Hormonal regulation of osteocyte perilacunar and canalicular remodeling in the hyp mouse model of x-linked hypophosphatemia. J Bone Miner Res 2018;33(3):499–509. [PubMed: 29083055]

21. Heveran CM, Rauff A, King KB, Carpenter RD, Ferguson VL. A new open-source tool for measuring 3D osteocyte lacunar geometries from confocal laser scanning microscopy reveals age-related changes to lacunar size and shape in cortical mouse bone. Bone 2018;110.

22. Lewis LMT, Xie Y, Hulbert MA, Campos R, Dallas MR, Bonewald LF, et al. Degeneration of the osteocyte network in the C57Bl/6 mouse model of aging. Aging (Albany NY) 2017;9(10):2190–208. [PubMed: 29074822]

23. Hemmatian H, Laurent MR, Bakker AD, Vanderschueren D, Klein-Nulend J, van Lenthe GH. Age-related changes in female mouse cortical bone microporosity. Bone 2018;113(April):1–8. [PubMed: 29738854]

24. Hemmatian H, Bakker AD, Klein-Nulend J, van Lenthe GH. Aging, Osteocytes, and Mechanotransduction. Curr Osteoporos Rep 2017;15(5):401–11. [PubMed: 28891009]

25. Ferguson VL, Ayers RA, Bateman TA, Simske SJ. Bone development and age-related bone loss in male C57BL/6J mice. Bone 2003;33(3):387–98. [PubMed: 13678781]

26. Zimmerman EA, Schaible E, Bale H, Barth HD, Tang SY, Reichert P, et al. Age-related changes in the plasticity and toughness of human cortical bone at multiple length scales. Proc Natl Acad Sci 2011;108(35):14416–21. [PubMed: 21873221]

27. Seeman E, Delmas PD. Bone Quality — The Material and Structural Basis of Bone Strength and Fragility. N Engl J Med 2006;354:2250–61. [PubMed: 16723616]

28. Halloran BP, Ferguson VL, Simske SJ, Burghardt A, Venton LL, Majumdar S. Changes in bone structure and mass with advancing age in the male C57BL/6J mouse. J Bone Miner Res 2002;17(6):1044–50. [PubMed: 12054159]

29. Lauretani F, Bandinelli S, Griswold ME, Maggio M, Semba R, Guralnik JM, et al. Longitudinal changes in BMD and bone geometry in a population-based study. J Bone Miner Res 2008;23(3):400–8. [PubMed: 17997708]

30. Yerramshetty JS, Lind C, Akkus O. The compositional and physicochemical homogeneity of male femoral cortex increases after the sixth decade. Bone 2006 12;39(6):1236–43. [PubMed: 16860007]

31. Currey JD. The relationship between the stiffness and the mineral content of bone. J Biomech 1969;2:477–80. [PubMed: 16335147]

32. Szulc P, Seeman E. Thinking inside and outside the envelopes of bone : Dedicated to PDD Osteoporos Int 2009;20(8):1281–8. [PubMed: 19590836]

33. Miyazaki-Anzai S, Levi M, Kratzer A, Ting TC, Lewis LB, Miyazaki M. Farnesoid × receptor activation prevents the development of vascular calcification in ApoE−/−mice with chronic kidney disease. Circ Res 2010;106(12):1807–17. [PubMed: 20431060]

34. Bouxsein ML, Boyd SK, Christiansen BA, Guldberg RE, Jepsen KJ, Müller R. Guidelines for assessment of bone microstructure in rodents using micro-computed tomography. J Bone Miner Res 2010;25(7):1468–86. [PubMed: 20533309]

35. Turner CH, Burr DB. Basic biomechanical measurements of bone: A tutorial. Bone 1993;14(4):595–608. [PubMed: 8274302]

36. Lau AG, Kindig MW, Kent RW. Morphology, distribution, mineral density and volume fraction of human calcified costal cartilage. Acta Biomater 2011;7(3):1202–9. [PubMed: 20974298]

37. Lau AG, Kindig MW, Salzar RS, Kent RW. Micromechanical modeling of calcifying human costal cartilage using the generalized method of cells. Acta Biomater 2015;18:226–35. [PubMed: 25712387]

38. Hexemer A, Bras W, Glossinger J, Schaible E, Gann E, Kirian R, et al. A SAXS/WAXS/GISAXS beamline with multilayer monochromator. J Phys Conf Ser 2010;247.

39. Barth HD, Zimmermann EA, Schaible E, Tang SY, Alliston T, Ritchie RO. Characterization of the effects of x-ray irradiation on the hierarchical structure and mechanical properties of human cortical bone. Biomaterials 2011;32(34):8892–904. [PubMed: 21885114]

40. Acevedo C, Bale H, Gludovatz B, Wat A, Tang SY, Wang M, et al. Alendronate treatment alters bone tissues at multiple structural levels in healthy canine cortical bone. Bone 2015;81:352–63. [PubMed: 26253333]

41. Abramoff MD, Magalhães PJ, Ram SJ. Biophotonics international. Biophotonics Int 2004;11(7):36–42.

42. Oliver WC, Pharr GM. An improved technique for determining hardness and elastic modulus using load and displacement sensing indentation experiments. Vol. 7, Journal of Materials Research 1992 p. 1564–83.

43. Bushby a. J, Ferguson VL, Boyde A. Nanoindentation of bone: Comparison of specimens tested in liquid and embedded in polymethylmethacrylate. J Mater Res 2004 3;19(01):249–59.

44. Bank RA, Beekman B, Verzijl N, De Roos JADM, Nico Sakkee A, Tekoppele JM. Sensitive fluorimetric quantitation of pyridinium and pentosidine crosslinks in biological samples in a single high-performance liquid chromatographic run. J Chromatogr B Biomed Appl 1997;703(1–2):37–44.

45. Oren TW, Botolin S, Williams A, Bucknell A, King KB. Arthroplasty in veterans: Analysis of cartilage, bone, serum, and synovial fluid reveals differences and similarities in osteoarthritis with and without comorbid diabetes. J Rehab Res Dev 2015;48(10):1195–210.

46. Bank RA, Jansen EJ, Beekman B, Te Koppele JM. Amino acid analysis by reverse-phase high-performance liquid chromatography: Improved derivatization and detection conditions with 9-fluorenylmethyl chloroformate. Anal Biochem 1996;240(2):167–76. [PubMed: 8811901]

47. Burr DB, Hooser M. Alterations to the en bloc basic fuchsin staining protocol for the demonstration of microdamage produced in vivo. Bone 1995;17(4):431–3. [PubMed: 8573418]

48. Feng JQ, Ye L, Schiavi S. Do osteocytes contribute to phosphate homeostasis? Curr Opin Nephrol Hypertens 2009;18(4):285–91. [PubMed: 19448536]

49. Feng JQ, Ward JM, Liu S, Lu Y, Xie Y, Yuan B, et al. Loss of DMP1 causes rickets and osteomalacia and identifies a role for osteocytes in mineral metabolism. Nat Genet 2006;38(11):1310–5. [PubMed: 17033621]

50. Komaba H, Fukagawa M. FGF23-parathyroid interaction: implications in chronic kidney disease. Kidney Int 2010;77(4):292–8. [PubMed: 20010546]

51. Boskey A, Coleman R. Aging and bone. J Dent Res 2010 12;89(12):1333–48. [PubMed: 20924069]

52. Wang X, Shen X, Li X, Mauli Agrawal C. Age-related changes in the collagen network and toughness of bone. Bone 2002;31(1):1–7. [PubMed: 12110404]

53. Faul F, Erdfelder E, Lang A-G, Buchner A. G*Power 3: A flexible statistical power analysis program for the social, behavioral, and biomedical sciences. IEEE Int Symp Inf Theory - Proc 2007;39(2):175–91.

54. Ritchie RO, Koester KJ, Ionova S, Yao W, Lane NE, Ager JW. Measurement of the toughness of bone: A tutorial with special reference to small animal studies. Bone 2008;43(5):798–812. [PubMed: 18647665]

55. Nyman JS, Roy A, Acuna RL, Gayle HJ, Reyes MJ, Tyler JH, et al. Age-related effect on the concentration of collagen crosslinks in human osteonal and interstitial bone tissue. Bone 2006;39(6):1210–7. [PubMed: 16962838]

56. Saito M, Fujii K, Mori Y, Marumo K. Role of collagen enzymatic and glycation induced cross-links as a determinant of bone quality in spontaneously diabetic WBN / Kob rats 2006;1514–23.

Highlights

- CKD and aging differentially affected bone material properties.

- CKD altered bone collagen nanomechanics.

- CKD and aging both reduced cortical and trabecular microarchitecture.

- Osteocyte lacunae may participate in phosphate mineral homeostasis in CKD.
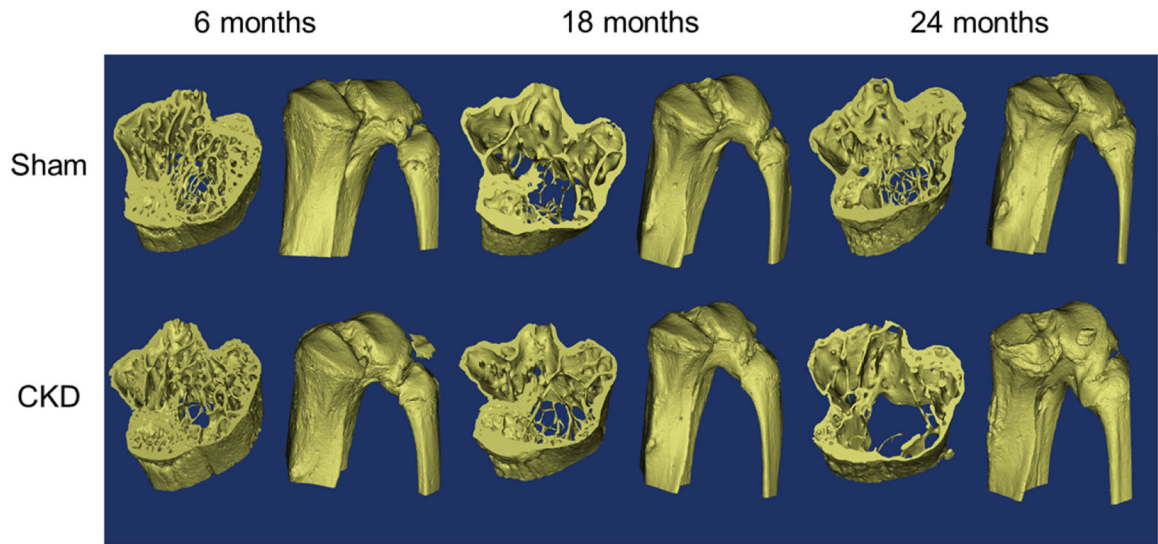
Figure 1: 3D Rendering of the proximal tibia.
Left: tibia region of analysis for microCT and FEA. Right: entire proximal tibia.
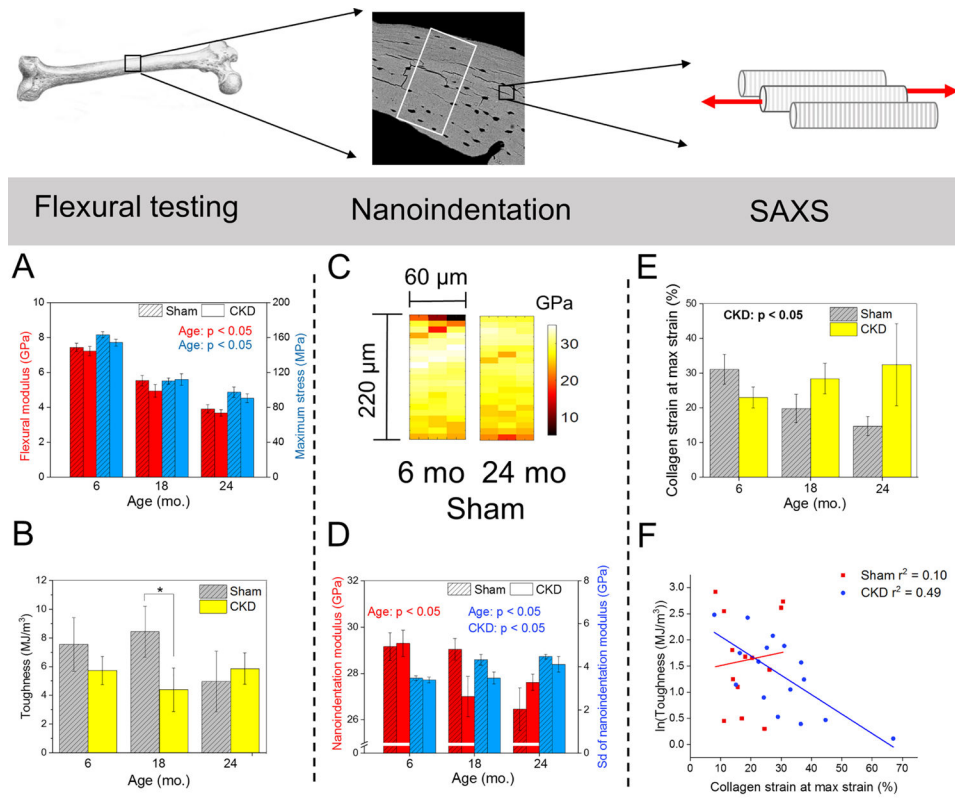
Figure 2

Figure 2: Bone quality changes with aging and CKD from the tissue-scale to the whole-bone scale.

At the whole-bone scale, A) aging reduces whole-femur strength and modulus while B) CKD reduces toughness only at middle-age. From C) representative nanoindentation maps, aging reduces modulus while aging and CKD have opposite effects on the standard deviation of modulus, an indicator of bone heterogeneity. At the nanoscale, E) CKD increases the SAXS percent collagen strain at maximum strain, which F) negatively correlates with toughness for CKD but not Sham mice. Significant main effects are noted with text, while significant post-hoc effects are indicated by *.

Table 1:

Serum and urine measures of kidney disease status at study end

	6 mo		18 mo		24 mo	
	Sham	**CKD**	**Sham**	**CKD**	**Sham**	**CKD**
Serum urea (mg/dL)	87.9 ± 5.84	152 ± 15.8	73.5 ± 6.76	212 ± 15.9	76.3 ± 11.5	188 ± 21.9
Age: NS						
CKD: p < 0.001						
Age × CKD: NS						
Urine urea (mg/dL)	8.94E3 ± 1.36E3	5.39E3 ± 0.599E3	8.28E3 ± 1.05E3	5.55E3 ± 0.633E3	9.48E3 ± 0.792E3	5.52E3 ± 0.846E3
Age: NS						
CKD: p < 0.001						
Age × CKD: NS						
Phosphate (mg/dL)	9.22 ± 1.77	12.7 ± 0.682	9.63 ± 0.890	12.3 ± 0.960	9.53 ± 0.830	11.9 ± 0.324
Age: NS						
CKD: p = 0.001						
Age × CKD: NS						
Calcium (mg/dL)	9.43 ± 0.282	7.50 ± 1.37	8.25 ± 0.554	9.16 ± 0.791	7.14 ± 1.14	8.78 ± 0.285
Age: NS						
CKD: NS						
Age × CKD: NS						
Parathyroid hormone (mg/dL)	165 ± 51.9	302 ± 113	180 ± 42.1	464 ± 76.3	228 ± 38.5	490 ± 114
Age: NS						
CKD: p = 0.002						
Age × CKD: NS						

Data are presented as mean +/− standard error of the mean. P-values for main effects of age and CKD as well as their interaction are reported in the left column. Serum urea, phosphate, and calcium were measured for 6 mo /Sham (n = 6), 6 mo/CKD (n = 7), 18 mo/Sham (n = 8), 18 mo/CKD (n = 10), 24 mo/Sham (n = 8), 24 mo/CKD (n = 8). PTH was assessed for 6 mo/Sham (n = 5), 6 mo/CKD (n = 5), 18 mo/Sham (n = 4), 18 mo/CKD (n = 6), 24 mo/Sham (n = 5), 24 mo/CKD (n = 5). Urine urea was measured for 6 mo /Sham (n = 6), 6 mo/CKD (n = 7), 18 mo/Sham (n = 7), 18 mo/CKD (n = 9), 24 mo/Sham (n = 7), 24 mo/CKD (n = 6).

Table 2:

Cortical microarchitecture from microCT

	6 mo		18 mo		24 mo	
	Sham **n = 5**	**CKD** **n = 7**	**Sham** **n = 8**	**CKD** **n = 9**	**Sham** **n = 8**	**CKD** **n = 8**
BV/TV	0.920 ± 0.00186	0.908 ± 0.00427	0.916 ± 0.00189	0.903 ± 0.00378	0.900 ± 0.00557	0.890 ± 0.00472
Age: p < 0.001						
CKD: **p = 0.001**						
Age × CKD: NS						
BA/TA	0.468 ± 0.00824	0.438 ± 0.0120	0.407 ± 0.00746	0.371 ± 0.00873	0.388 ± 0.00942	0.335 ± 0.00744
Age: p < 0.001						
CKD: p < 0.001						
Age × CKD: NS						
Ct.Po	8.05 ± 0.186	9.21 ± 0.427	8.44 ± 0.189	9.72 ± 0.378	9.98 ± 0.557	11.0 ± 0.472
Age: p < 0.001						
CKD: p < 0.001						
Age × CKD: NS						
Ct. Th (mm)	0.202 ± 0.00186	0.187 ± 0.00525	0.189 ± 0.00385	0.168 ± 0.00473	0.198 ± 0.00610	0.162 ± 0.00427
Age: p = 0.004						
CKD: p < 0.001						
Age × CKD: NS						
TMD (mg HA /cm^3)	$1.04E3 \pm 9.13$	$1.02E2 \pm 4.08$	$1.06E2 \pm 6.58$	$1.04E2 \pm 6.16$	$1.07E2 \pm 2.82$	$1.04E2 \pm 6.42$
Age: p = 0.001						
CKD: p < 0.001						
Age × CKD: NS						
I$_{ML}$(mm^4)	0.138 ± 0.00804	0.132 ± 0.00864	0.178 ± 0.0137	0.138 ± 0.00533 [*]	0.240 ± 0.00844	0.175 ± 0.0145 [*]
Age: p < 0.001						
CKD: p < 0.001				p = 0.004		p < 0.001
Age × CKD: p < 0.05				−22.5%		−27.1%
pMOI	0.446 ± 0.0221	0.406 ± 0.0200	0.542 ± 0.0366	0.433 ± 0.0145	0.683 ± 0.0282	0.535 ± 0.0374
Age: p < 0.001						
CKD: p < 0.001						
Age × CKD: NS						

Data are presented as mean +/− standard error of the mean. P-values for main effects of age and CKD as well as their interaction are reported in the left column. Post-hoc testing was performed for measures with a significant interaction between age and CKD.

[*] Indicates significant difference between Sham and CKD at the same age (p < 0.017, Bonferroni-adjusted critical α), while percent differences between Sham and CKD are noted when p < 0.05.

Table 3:

Trabecular microarchitecture from microCT

	6 mo		18 mo		24 mo	
	Sham **n = 5**	**CKD** **n = 7**	**Sham** **n = 8**	**CKD** **n = 9**	**Sham** **n = 8**	**CKD** **n = 8**
BV/TV	0.103 ± 0.00682	0.0962 ± 0.0107	0.0599 ± 0.00469	0.0441 ± 0.00511	0.0637 ± 0.00650	0.0376 ± 0.00271
Age: p < 0.001						
CKD: p < 0.001						
Age × CKD: NS						
Conn.D (1/mm³)	54.2 ± 6.14	69.3 ± 13.1	20.4 ± 4.11	16.44 ± 5.70	28.4 ± 5.48	22.98 ± 2.49
Age: p < 0.001						
CKD: NS						
Age × CKD: NS						
Tb.N (1/mm)	4.02 ± 0.115	3.84 ± 0.221	2.96 ± 0.0739	2.77 ± 0.144	2.74 ± 0.132	2.33 ± 0.108
Age: p < 0.001						
CKD: p = 0.032						
Age × CKD: NS						
Tb.Sp (mm)	0.244 ± 0.00829	0.263 ± 0.0168	0.337 ± 0.00895	0.371 ± 0.0225	0.370 ± 0.0204	0.441 ± 0.0222
Age: p < 0.001						
CKD: p = 0.013						
Age × CKD: NS						
Tb.Th (mm)	0.0488 ± 0.00115	0.0429 ± 0.00130	0.0485 ± 0.00102	0.0454 ± 0.00185	0.0464 ± 0.00194	0.0403 ± 0.00146
Age: NS						
CKD: p < 0.001						
Age × CKD: NS						
vBMD (mg HA/cm³)	126 ± 7.79	117 ± 13.0	77.6 ± 5.16	54.4 ± 6.86	76.0 ± 7.58	42.7 ± 3.03
Age: p < 0.001						
CKD: p < 0.001						
Age × CKD: NS						

Data are presented as mean +/− standard error of the mean. P-values for main effects of age and CKD as well as their interaction are reported in the left column.

Table 4:

Whole-bone mechanical and material properties from three-point bending and FEA

	6 mo		18 mo		24 mo	
	Sham **n = 5**	**CKD** **n = 7**	**Sham** **n = 8**	**CKD** **n = 9**	**Sham** **n = 8**	**CKD** **n = 8**
Stiffness (N/mm) *Age: p = 0.009* *CKD: p < 0.001* Age × CKD: NS	99.2 ± 5.11	88.5 ± 4.68	91.5 ± 6.03	64.4 ± 6.39	83.2 ± 6.93	62.7 ± 6.23
Modulus (GPa) *Age: p < 0.001* CKD: NS Age × CKD: NS	7.44 ± 0.237	7.22 ± 0.266	5.53 ± 0.307	4.95 ± 0.360	3.92 ± 0.240	3.69 ± 0.186
Yield Stress (MPa) *Age: p < 0.001* CKD: NS Age × CKD: NS	132 ± 10.7	127 ± 4.74	82.2 ± 6.51	76.0 ± 10.2	65.9 ± 7.46	66.1 ± 4.74
Maximum Stress (MPa) *Age: p < 0.001* CKD: NS Age × CKD: NS	163 ± 3.55	154 ± 3.88	110 ± 3.62	112 ± 6.53	97.4 ± 5.99	90.5 ± 4.81
Work to Fracture (mJ) Age: p > 0.05 *CKD: p = 0.041* Age × CKD: NS	6.40 ± 1.48	4.47 ± 0.735	8.51 ± 1.25	3.87 ± 1.22	5.11 ± 1.89	4.53 ± 1.03
Toughness (MJ/m³) Age: NS CKD: NS *Age × CKD: p = 0.011*	7.54 ± 1.86	4.87 ± 0.582	8.43 ± 1.78	4.39 ± 1.51 [*] p = 0.022 −47.9%	3.03 ± 0.982	5.86 ± 1.10 p = 0.046 +93.9%
Post-Yield Displacement (mm) Age: NS CKD: NS Age × CKD: NS	0.342 ± 0.0954	0.195 ± 0.0216	0.947 ± 0.227	0.535 ± 0.226	0.250 ± 0.0672	0.481 ± 0.117
FEA Stiffness (N/mm) *Age: p < 0.001* *CKD: p < 0.001* Age × CKD: NS	9680 ± 305	8750 ± 595	7780 ± 254	6440 ± 289	7840 ± 503	6550 ± 454

Data are presented as mean +/− standard error of the mean. P-values for main effects of age and CKD as well as their interaction are reported in the left column. Post-hoc testing was performed for measures with a significant interaction between age and CKD.

*Indicates significant difference between Sham and CKD at the same age (p < 0.017, Bonferroni-adjusted critical α), while percent differences between Sham and CKD are noted when p < 0.05.

Table 5:

Mean microscale material properties from nanoindentation and Raman spectroscopy

	6 mo		18 mo		24 mo	
	Sham **n = 6**	**CKD** **n = 6**	**Sham** **n = 6**	**CKD** **n = 6**	**Sham** **n = 6**	**CKD** **n = 6**
E_r **(GPa)**	29.2 ± 0.594	29.3 ± 0.567	29.0 ± 0.462	27.0 ± 0.872	26.5 ± 0.918	26.7 ± 0.962
Age: p = 0.006						
CKD: NS						
Age × CKD: NS						
ν_1 **phosphate: (proline +hydroxyproline)**	19.2 ± 3.69	17.0 ±2.97	20.2 ± 1.74	28.0± 6.69	21.3 ± 3.71	14.4 ± 1.45
Age: NS						
CKD: NS						
Age × CKD: NS						
Carbonate:phosphate	9.35E-2 ± 0.818E-2	10.0E-2 ± 1.07E-2	10.1E-1 ± 0.957E-2	10.1E-2 ± 0.997E-2	10.6E-2 ± 0.944E-2	9.91E-2 ± 0.905E-2
Age: NS						
CKD: NS						
Age × CKD: NS						
Crystallinity	5.78E-2 ± 6.16E-4	5.83E-2 ± 8.54E-4	5.713E-2 ± 4.89E-4	5.81E-2 ± 7.66E-4	5.64E-2 ± 3.75E-4	5.79E-2 ± 8.87E-4
Age: NS						
CKD: NS						
Age × CKD: NS						
stdev E_r (GPa)	3.47 ± 0.108	3.40 ± 0.128	4.34 ± 0.252	3.48 ± 0.278	4.48 ± 0.107	4.12 ± 0.359
Age: p = 0.004						
CKD: p = 0.032						
Age × CKD: NS						
stdev ν_1 phosphate: (proline +hydroxyproline)	10.8 ± 2.83	11.0 ± 3.38	8.87 ± 1.05	19.5 ± 6.73	15.5 ± 5.12	5.18 ± 0.819
Age: NS						
CKD: NS						
Age × CKD: NS						
Stdev carbonate:phosphate	11.0E-3 ± 0.517E-3	12.0E-3 ± 1.23E-3	9.46E-3 ± 0.860E-3	11.3E-3 ± 1.53E-3	10.3E-3 ± 0.742E-3	13.4E-3 ± 1.74E-3
Age: NS						
CKD: NS						
Age × CKD: NS						
stdev crystallinity	1.48E-3 ± 0.158E-3	1.17E-3 ± 0.0930E-3	1.52E-3 ± 0.171E-3	1.09E-3 ± 0.154E-3	1.14E-3 ± 0.121E-3	1.19E-3 ± 0.0760E-3
Age: NS						

	6 mo		18 mo		24 mo	
	Sham **n = 6**	**CKD** **n = 6**	**Sham** **n = 6**	**CKD** **n = 6**	**Sham** **n = 6**	**CKD** **n = 6**
CKD: p = 0.048						
Age × CKD: NS						

Data are presented as mean +/− standard error of the mean. P-values for main effects of age and CKD as well as their interaction are reported in the left column.

Table 6:

Tissue and collagen strain from SAXS

	6 mo		18 mo		24 mo	
	Sham **n = 5**	**CKD** **n = 7**	**Sham** **n = 4**	**CKD** **n = 7**	**Sham** **n = 5**	**CKD** **n = 4**
Modulus (GPa)	12.1 ± 2.55	13.2 ± 2.21	10.3 ± 1.05	14.7 ± 1.58	10.5 ± 1.89	12.5 ± 3.29
Age: NS						
CKD: NS						
Age × CKD: NS						
Tissue yield stress (MPa)	56.8± 0.892	50.9 ± 2.80	48.7 ± 2.83	38.9 ± 6.97	39.6 ± 5.87	44.3 ± 3.34
Age: p = 0.046						
CKD: NS						
Age × CKD: NS						
Tissue yield strain	0.743 ± 0.0900	0.631 ± 0.0528	0.681 ± 0.0313	0.416 ± 0.0569	0.551 ± 0.101	0.559 ± 0.0718
Age: NS						
CKD: NS						
Age × CKD: NS						
Tissue maximum stress (MPa)	74.3 ± 5.42	61.6 ± 2.71	58.6± 3.28	44.1± 8.64	47.0 ± 6.72	52.3 ± 5.26
Age: p = 0.011						
CKD: p > 0.05						
Age × CKD: p > 0.05						
Tissue maximum strain	2.13 ± 0.485	1.21 ± 0.102	1.45 ± 0.286	0.784 ± 0.186	0.958 ± 0.165	0.111 ± 0.235
Age: p = 0.033						
CKD: p = 0.030						
Age × CKD: NS						
Collagen strain at yield strain	0.219 ± 0.0277	0.272 ± 0.0508	0.208 ± 0.0389	0.180 ± 0.0403	0.171 ± 0.0575	0.199± 0.0445
Age: NS						
CKD: NS						
Age × CKD: NS						
Collagen strain at maximum strain	0.465± 0.0899	0.354 ± 0.0520	0.267 ± 0.0485	0.222 ± 0.0625	0.168 ± 0.0575	0.331 ± 0.0933
Age: p = 0.033						
CKD: p > 0.05						
Age × CKD: p > 0.05						
Percent collagen strain at yield	30.4 ± 2.96	45.6 ± 9.78	30.4 ± 5.23	35.4 ± 5.66	24.5 ± 6.14	34.7 ± 7.43
Age: NS						
CKD: NS						
Age × CKD: NS						

	6 mo		18 mo		24 mo	
	Sham **n = 5**	**CKD** **n = 7**	**Sham** **n = 4**	**CKD** **n = 7**	**Sham** **n = 5**	**CKD** **n = 4**
Percent collagen strain at maximum strain, %ColMax	23.0 ± 3.00	31.1 ± 4.32	19.8 ± 4.08	28.4 ± 4.38	14.7 ± 2.75	32.4 ± 11.8
Age: NS						
CKD: p = 0.014						
Age × CKD: NS						

Data are presented as mean +/− standard error of the mean. P-values for main effects of age and CKD as well as their interaction are reported in the left column.

Table 7:

Collagen crosslink assessments

	6 mo		18 mo		24 mo	
	Sham **n = 4**	**CKD** **n = 7**	**Sham** **n = 6**	**CKD** **n = 9**	**Sham** **n = 7**	**CKD** **n = 8**
HP (mol / mol collagen)	2.17 ± 0.39	2.15 ± 0.28	2.44 ± 0.25	2.57 ± 0.19	2.97 ± 0.25	2.29 ± 0.25
Age: NS						
CKD: NS						
Age × CKD: NS						
LP (mol / mol collagen)	0.29 ± 0.02	0.23 ± 0.02	0.30 ± 0.02	0.30 ± 0.02	0.31 ± 0.01	0.28 ± 0.01
Age: NS						
CKD: p = 0.056						
Age × CKD: NS						
Pentosidine (mol / mol collagen)	1.39 ± 0.43	1.57 ± 0.26	2.42 ± 0.75	2.11 ± 0.53	2.59 ± 0.59	2.62 ± 0.35
Age: NS						
CKD: NS						
Age × CKD: NS						
Total fluorescent AGEs	188 ± 12.0	204 ± 18	321 ± 89.3	206 ± 34.0	242 ± 55.9	219 ± 33.6
Age: NS						
CKD: NS						
Age × CKD: NS						

Data are presented as mean +/− standard error of the mean. P-values for main effects of age and CKD as well as their interaction are reported in the left column.

Table 8:

3D osteocyte lacunar geometries from confocal laser scanning microscopy

	6 mo		18 mo		24 mo	
	Sham **n = 6**	**CKD** **n = 5**	**Sham** **n = 7**	**CKD** **n = 6**	**Sham** **n = 6**	**CKD** **n = 5**
Volume (μm^3)	488 ± 33.9	440 ± 64.1	390 ± 68.8	299 ± 34.5	294 ± 27.8	393 ± 62.3
Age: p = 0.044						
CKD: NS						
Age × CKD: NS						
Surface area (μm^2)	361 ± 14.6	334 ± 31.5	300 ± 35.3	249 ± 19.0	251 ± 18.2	308 ± 34.7
Age: p = 0.021						
CKD: NS						
Age × CKD: NS						
Sphericity	0.283 ± 0.00233	0.300 ± 0.00462	0.313 ± 0.00853	0.335 ± 0.00655	0.329 ± 0.0115	0.304 ± 0.0100
Age: p = 0.001						
CKD: NS						p = 0.042
Age × CKD: p = 0.014						−7.60%
Closest center of mass	19.9 ±	20.3 ±	20.0 ± 0.499	20.0 ± 0.415	21.2 ± 0.540	20.5 ±
(μm)	0.367	0.478				0.520
Age: NS						
CKD: NS						
Age × CKD: NS						
Span theta (degrees)	17.6 ± 1.23	19.9 ± 2.58	23.9 ± 2.21	25.2 ± 4.05	27.2 ± 2.94	29.8 ± 5.58
Age: p = 0.023						
CKD: NS						
Age × CKD: NS						
Oblateness	−0.316 ± 0.0344	−0.182 ± 0.0614	−0.204 ± 0.0476	−0.207 ± 0.0761	−0.0875 ± 0.0333	−0.121 ± 0.0356
Age: p = 0.029						
CKD: NS						
Age × CKD: NS						
Lacunar number density **($1/\mu m^3$)**	3.06E-5 ± 0.280E-5	2.50E-5 ± 0.312E-5	2.30E-5 ± 0.240E-5	1.97E-5 ± 0.193E-5	1.91E-5 ± 0.164E-5	2.40E-5 ± 0.264E-5
Age: p = 0.022						
CKD: NS						
Age × CKD: NS						

Data are presented as mean +/− standard error of the mean. Post-hoc testing was performed for measures with a significant interaction between age and CKD.

[*]
Indicates significant difference between Sham and CKD at the same age (p < 0.017, Bonferroni-adjusted critical α), while percent differences between Sham and CKD are noted when p < 0.05.